

RESEARCH ARTICLE

Open Access



ISO-FLUCS: symmetrization of optofluidic manipulations in quasi-isothermal micro-environments

Antonio Minopoli^{1,3}, Susan Wagner^{1,3}, Elena Erben^{1,3}, Weida Liao², Iliya D. Stoev^{1,3}, Eric Lauga² and Moritz Kreysing^{1,3,4*}

Abstract

Recently, it has been demonstrated that thermoviscous flows can be used for a range of fine micromanipulations, such as moving the cytoplasm of cells and developing embryos, intracellular rheology, and femtonewton-range force measurements. These flows, also known as focused-light-induced cytoplasmic streaming (FLUCS), are induced by mid-infrared laser scanning of a temperature spot through the sample. However, localized laser scanning can inflict temperature perturbations of several Kelvins on the sample, potentially eliciting unspecific biological responses. In this study, we demonstrate how exploiting symmetry relations during laser scanning effectively disentangles laser heating and flow induction. We introduce flow-neutral scan sequences that use dynamic photothermal stimuli and spatiotemporal symmetry relations of scanning bridging up to three distinct time scales. We leverage further insights from a recently published analytical model of flow fields to present quasi-homogenous temperature distributions that leave flow lines and their local and directed character largely invariant. We present practical, intuitive solutions through predesigned sets of scan lines with near isothermal distributions and demonstrate that they are sufficient to generate and control flows in *Caenorhabditis elegans* embryos on a magnitude well in excess of endogenous flow velocities. Our results enable the separation of two previously tightly linked classes of physical stimuli, introduce a new, even less invasive standard for performing FLUCS perturbations, and pave the way for new unexplored avenues in the fields of soft matter and biomedicine.

*Correspondence:

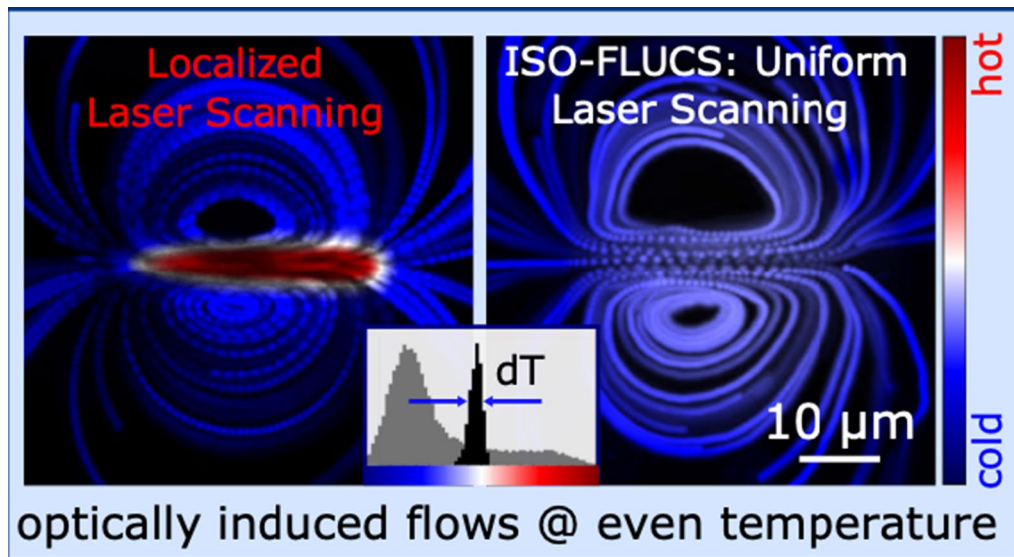
Moritz Kreysing
moritz.kreysing@kit.edu

Full list of author information is available at the end of the article



© The Author(s) 2023. **Open Access** This article is licensed under a Creative Commons Attribution 4.0 International License, which permits use, sharing, adaptation, distribution and reproduction in any medium or format, as long as you give appropriate credit to the original author(s) and the source, provide a link to the Creative Commons licence, and indicate if changes were made. The images or other third party material in this article are included in the article's Creative Commons licence, unless indicated otherwise in a credit line to the material. If material is not included in the article's Creative Commons licence and your intended use is not permitted by statutory regulation or exceeds the permitted use, you will need to obtain permission directly from the copyright holder. To view a copy of this licence, visit <http://creativecommons.org/licenses/by/4.0/>.

Graphical Abstract



1 Introduction

Micromanipulation techniques are widely adopted in materials science, colloidal physics and life sciences for a wide variety of applications, ranging from nanostructure assembly [1, 2] and particle trapping [3, 4] to spatio-temporal analysis of cell organization [5–8]. Recently, we have introduced optically induced thermoviscous flows [9, 10], i.e. focused-light-induced cytoplasmic streaming (FLUCS), to manipulate the cytoplasm in cells and developing embryos [11–15]. Thermoviscous flows arise from the complex interplay between thermal expansion and temperature induced viscosity changes when repeatedly moving a heating point stimulus through a thin film of fluid [9]. Specifically, the localized heating generated by scanning the IR-laser spot through the sample induces a local small change in the density and viscosity of the fluid, resulting in a locally compressible fluid flow with a net transport of tracers [9, 10].

Additionally, contact-free positioning of polystyrene microbeads on the nanoscale level [16] and high-sensitivity force measurements in the femtonewton-range [17, 18] were achieved by implementing a feedback-based control. Although FLUCS has the advantage of generating directional flows with reduced invasiveness and fully haptic control, samples still experience a significant temperature modulation (ca. 3.5 K when compensated by ambient cooling) (Fig. 1b), which could have implications for highly heat-sensitive systems, such as thermosensitive

mammalian cells [19–21], thermolabile oocytes [22], and thermoregulated gill tissues [23].

In our current work, we show that it is possible to use a step-by-step optical strategy to disentangle laser-induced flows and heating. We make use of previously disregarded degrees of freedom that accompany the optical generation of flow fields (Fig. 1a). Specifically, the temperature distribution can be significantly homogenized over the region of interest (ROI) by introducing additional counter-directed paths, symmetrically arranged around the desired trajectory. Additionally, we exploit symmetry relations in performing scanning on up to three distinct time scales. This leads to locally homogeneous temperature distributions, while inducing directional flows with flow lines that are largely unaltered (Fig. 1c). Simultaneously, the sample is cooled to the required temperature with an external Peltier cooling system. We demonstrate that this technology, which we call isothermal FLUCS (ISO-FLUCS), is associated with at least tenfold reduction in heating while achieving thermoviscous flows well in excess of endogenous streaming in *Caenorhabditis elegans* zygotes. Given its drastically reduced heating impact while retaining FLUCS' main features (directional, versatile, non-invasive, haptic), we believe that ISO-FLUCS will become the new standard for these optical manipulations in highly temperature-sensitive systems in biology and materials science.

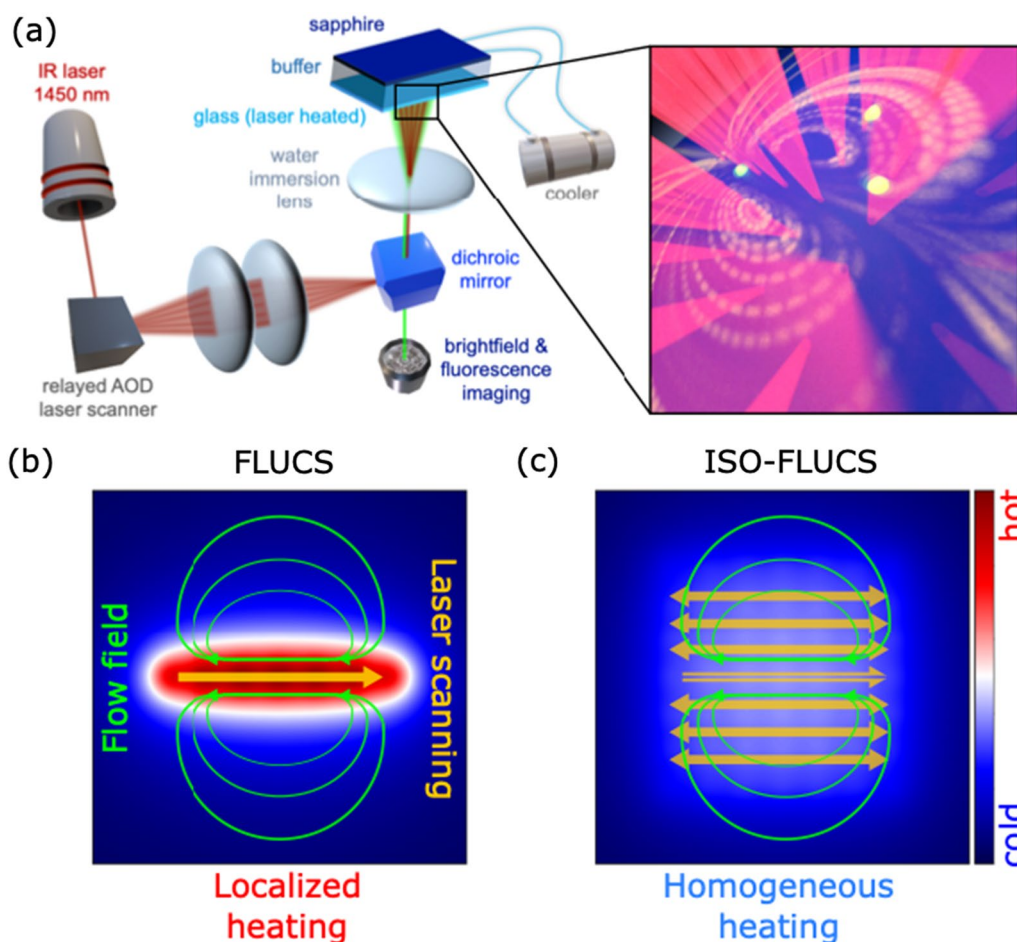


Fig. 1 ISO-FLUCS: homogeneous laser scanning for an even time-averaged temperature distribution on the sample while still inducing net thermoviscous flows. **a** Optical layout of the FLUCS setup capable of simultaneous imaging and inducing intracellular flows. The flow-inducing infrared laser beam is *x/y*-scanned by an acousto-optic deflector (AOD) and relayed by a telescope onto a dichroic mirror, thereby combining it with the imaging path. Both are coupled to the back focal plane of a high-numerical-aperture, custom-coated microscope objective lens. Flows are generated by laser-induced relative temperature increase within the region of interest (ROI). The absolute temperature within the ROI is controlled through adjunctive heating or cooling of the whole sample by Peltier elements connected to a highly conducting sapphire slide. **b** Simulated temperature distribution produced by repeatedly scanning an infrared laser along a single line. The highly localized heating entails a relatively strong temperature increase along the track. **c** A two-step scan pattern heats the entire ROI uniformly: forward followed by backward scans aim to cancel net flows everywhere except on the ‘flow line’ (middle line) where scans point in the same direction and their effects are reinforced

2 Results and discussion

2.1 ISO-FLUCS patterning inspired by heuristic simulations

To obtain the performance of standard FLUCS without the induction of large temperature gradients, it is necessary to uncouple temperature from thermoviscous-flow induction. One way to achieve this is to homogenize the temperature over a wider area by creating additional scan paths. Thermoviscous flow speeds depend primarily on the frequency with which the laser scans along a given path rather than on the velocity of the laser-heated temperature profile. Therefore, it should be possible to accelerate the primary scan pattern, thereby compressing the scan signal to occupy only a fraction of the original

period. This effective reduction of the duty cycle would allow us to introduce secondary scan points that would spread the heating over a wider area in a given duty cycle, effectively homogenizing the temperature. In the following, we introduce strategies relying on this previously unexploited degree of freedom to complement even complex primary scan patterns with secondary heating stimuli, thereby yielding a near isothermal temperature distribution.

To obtain a first benchmark of these additional patterns, we used heuristic simulations based on experimental data of the temperature distribution around a given point. First, we measured the fluorescence intensity of

Rhodamine B—a fluorescent dye whose quantum yield decreases as the temperature increases—at different temperatures in the range 21–28 °C. Additional file 1: Fig. S1 shows the calibration curve in which the fluorescence intensity of Rhodamine B is linearly related to the temperature change with the proportionality constant -0.0074 K^{-1} . To determine the temperature profile of our beam, we then evaluated the time-averaged reduction in fluorescence intensity experienced by Rhodamine B when repeatedly visited by the beam spot (Fig. 2a). Figure 2b shows the cross-section of the Rhodamine B intensity measured across the scan track; the data were fitted by the Cauchy-Lorentz equation:

$$y = \frac{a}{\pi(bx^2 + a^2)} + c, \quad (1)$$

where $a = -10.21 \pm 0.05$, $b = (9.3 \pm 0.2) \times 10^{-2} \mu\text{m}^{-2}$ and $c = 0.966 \pm 0.003$. In addition, we measured the peak temperature experienced by the sample from the stroboscopic reconstruction of the temperature cycle along the scan path (see Additional file 1: Fig. S2 for more details). Sub-millisecond temperature increases of $+5 \text{ °C}$ and

$+2 \text{ °C}$ were measured by scanning the laser spot along a single line ($70\text{-}\mu\text{m}$ long) and multiple lines (the total length of the pattern is $400 \mu\text{m}$), respectively, comparable with those measured previously [12].

Similar to the use of Green's functions in differential equations, where the response of complex systems is written as the superposition of responses to a point stimuli, we simulated the time-averaged temperature distribution of a given scan pattern (e.g., a spiral) by considering the linear superposition of heating point stimuli (Fig. 2c) [24, 25]. The corresponding histogram in Fig. 2d reveals a relatively broad temperature range with a standard deviation (*SD*) of 2.1 °C . Thus, this relatively wide temperature distribution has to be narrowed by conveniently including additional heating point stimuli in the scan pattern.

To improve the heating homogeneity over the sample by including additional heating point stimuli, their optimal distance from each other should be defined. Thus, we evaluated the temperature distribution generated by two heat spots with increasing separation. The optimal distance depends on the beam parameters (e.g., spot size, spot shape, light intensity distribution). Although a more

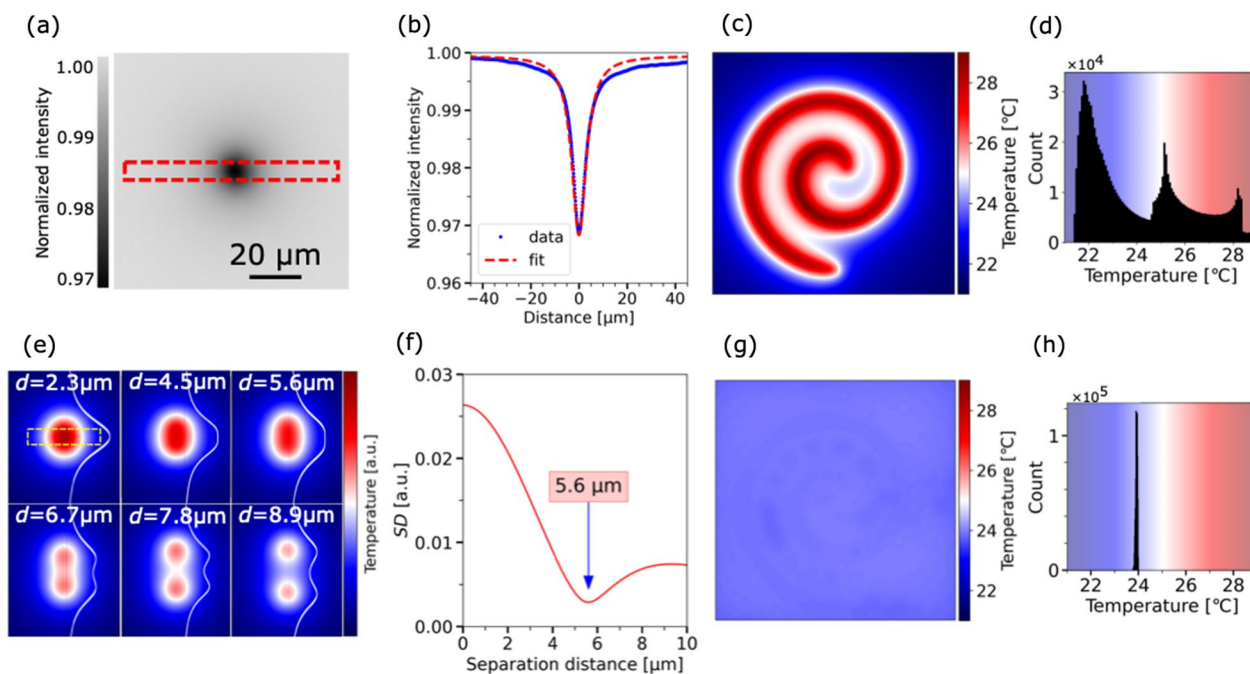


Fig. 2 Semi-empirical simulations to determine the scan pattern with minimal temperature impact. **a** Time-averaged fluorescence image of Rhodamine B when exposed to the IR laser. The red dashed rectangle highlights the region of interest (ROI) where the intensity cross-section was evaluated. **b** Temperature profile of a heat spot measured from Rhodamine B fluorescence in glycerol/water solution. The data are best fitted by a Cauchy-Lorentz curve (Eq. 1). **c** Simulated temperature distribution induced by a spiral pattern and **d** corresponding temperature histogram. **e** Simulated temperature distributions induced by two heat spots placed at different separation distances. The corresponding intensity cross-sections (solid white curves) reveal a relatively homogeneous temperature profile within the ROI (yellow dashed rectangle) at approximately $5.6\text{-}\mu\text{m}$ separation distance. **f** Standard deviation of the temperature distribution measured within the ROI in panel **e** as a function of the separation distance between the heat spots indicates an optimal distance of $5.6 \mu\text{m}$. **g** Simulated temperature distribution induced by a spiral ISO-FLUCS pattern and **h** corresponding temperature histogram

general model would be desirable to theoretically predict the optimal separation distance, it would go beyond the scope of the present work. However, the concept behind the proposed approach can be easily transferred and used as a guideline for any laser setting since the beam profile (measured experimentally in this work) is given as an input and can be potentially outlined once the beam geometry is known. Figure 2e shows that the temperature gradient flattens as the separation increases and a trend reversal arises as the heat spots move further away from each other. This is even more evident when the SD of the temperature is evaluated within the ROI (dashed yellow box). Specifically, the SD sharply decreases as the separation distance increases up to $5.6\ \mu\text{m}$ and then increases at larger distances (Fig. 2f). Indeed, at distances smaller than the half width at half maximum of the temperature cross-section, the heat load accumulates in the overlapping region, giving rise to a more pronounced temperature gradient. On the contrary, a colder gap arises in the middle when the two heat spots are placed at larger separation distances. Thus, the optimal distance between two heat spots in our system is $5.6\ \mu\text{m}$.

Once the optimal separation had been defined, we used heuristic simulations to obtain a preliminary picture of the additional pattern that would improve the temperature homogeneity within the entire ROI. Specifically, individual heating points were iteratively included in the ROI so that the lattice period was $5.6\ \mu\text{m}$ and the SD of the resulting temperature distribution was minimized (Fig. 2g). The corresponding histogram in Fig. 2h shows a very narrow temperature distribution with an SD of $0.1\ ^\circ\text{C}$. Then, the heating spots were clustered according to their distance from the defined path (Additional file 1: Fig. S3). As a result, this pipeline defines a set of points that are amenable to scanning as a benchmark for reducing the temperature stress in the ROI generated by any given pattern.

2.2 Temporal sequence of scan pattern to separate flows and heating

Next, we asked if it would be possible to design temporal scan sequences such that (i) all points required for homogeneous heating are visited with the same frequency during one scan period, and (ii) the desired flow fields are still induced. It is important that the scan frequency is high enough so that the time delay between visiting the same point in two consecutive periods is significantly lower than the characteristic timescale of the thermoviscous phenomenon. As a proof of concept, we considered a simple ISO-FLUCS pattern consisting of seven parallel and equidistant lines, and we attempted to induce a net flow only along the middle line.

To achieve this, the thermoviscous flows generated by all the other six lines must be cancelled. To this end, we adopted a two-step scanning $A(x,t)$ (Fig. 3a) in which the lines were sequentially scanned in both directions to counteract the thermoviscous flows—except for the middle line, which was scanned twice in the same direction. This strategy successfully induced a net flow along the desired path at the expense of a distortion in the particle trajectories (Fig. 3b). We speculated that the line-by-line scanning might introduce additional flow components orthogonal to the main direction of scanning. To visualize the flow field, we used fluorescent polystyrene beads ($1\text{-}\mu\text{m}$ diameter) dispersed in a highly viscous medium (pure honey) to suppress the particle diffusion. Full details on the pattern geometry and scan sequence are reported in Additional file 1: Table S1 and Additional file 2: Video S1. Thus, although this strategy allows individual points to be visited with the same frequency and successfully created a net flow along the middle line, the overall flow fields are distorted.

2.3 Multi-timescale symmetrization of a scan sequence to restore broken flow-field symmetries

To fix the distortions in the flow field, we developed a powerful approach that exploits symmetry relations of scanning on two distinct time scales. When we sequentially added a time-inverted scanning loop $A(x,-t)$ (line-by-line scanning from bottom to top) to the previous one $A(x,t)$, the resulting pattern $A(x,t) + A(x,-t)$ restored the broken symmetry with respect to x as a mirror axis. However, a stretched field emerged due to the broken symmetry that was still present with respect to y as a mirror axis (Fig. 3c). Indeed, the laser sequentially scanned the lines from left to right (LR) and from right to left (RL) (except for the middle line always scanned RL) in both the scan periods $A(x,t)$ and $A(x,-t)$. Full details are reported in Additional file 1: Table S1 and Additional file 2: Video S1.

In an attempt to correct this asymmetric field, we included two x -inverted scanning loops to the previous y -symmetric pattern. Now, the pattern consisted of four scanning periods: (i) $A(x,t)$, the lines are sequentially scanned from left to right and from right to left (LR-RL) while the pattern from top to bottom (TB); (ii) $A(x,-t)$, the lines are scanned LR-RL, while the pattern from bottom to top (BT); (iii) $A(-x,t)$ the lines are sequentially scanned from right to left and from left to right (RL-LR) while the pattern TB; (iv) $A(-x,-t)$, the lines are scanned RL-LR, while the pattern BT (except for the middle line always scanned RL). Full details are reported in Additional file 1: Table S1 and Additional file 2: Video S1. The resulting field had a restored symmetry with respect to x as a mirror axis. However, we observed a slight distortion when comparing both sides of the x -axis (Fig. 3d).

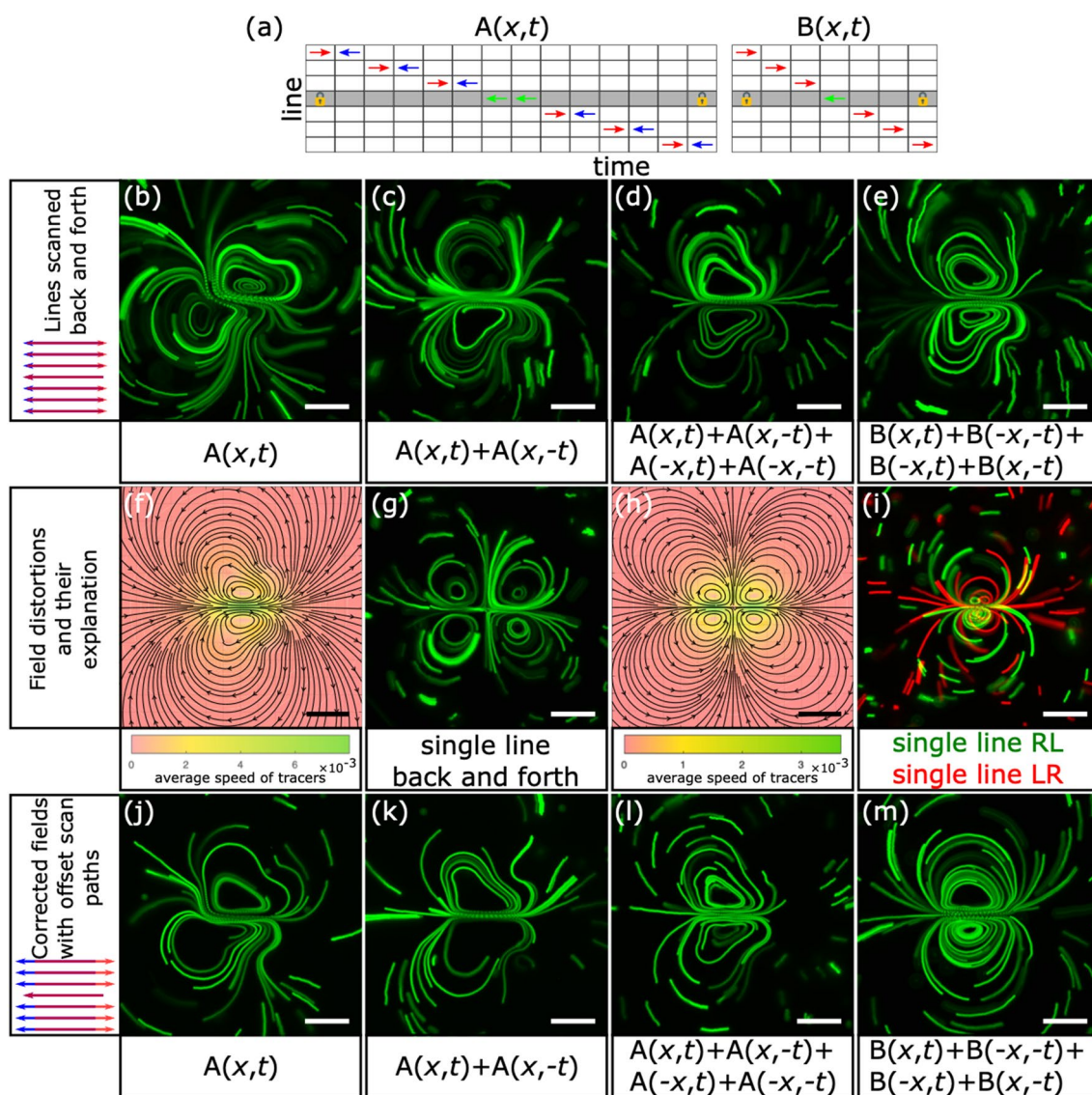


Fig. 3 Symmetrization of the scan pattern resolves distortions of the flow field. Maximum intensity projections over time show flow trajectories of fluorescent beads driven by different scan patterns. **a** Diagram of the temporal scanning units used to compose the ISO-FLUCS patterns. **b** Distorted flow field obtained by scanning a pattern with x and y broken symmetry. **c** Asymmetric flow field obtained by scanning a pattern with x broken symmetry. **d** Asymmetric flow field obtained by scanning a symmetric pattern. **e** Asymmetric flow field obtained by scanning a symmetric pattern with minimal cost. **f** Theoretical leading-order trajectories of tracers induced by a Gaussian heat spot scanning the same pattern as for panel **e**, but with an offset of 2 μm included between the forward and reverse paths. The dimensionless speed of the tracers (see Sect. 4.7 for details), averaged over the total time taken for the scan pattern, is indicated as a color map. **g** Quadrupolar flow field obtained by experimentally scanning a single line (33- μm long) back and forth. **h** Theoretical leading-order trajectories of tracers induced by a Gaussian heat spot scanning the same pattern as for panel **g**, but with an offset of 2 μm included between the forward and reverse paths. The dimensionless predicted speed of the tracers (see Sect. 4.7 for details), averaged over the time taken for the scan pattern, is indicated as a color map. **i** Montage of the dipolar fields obtained by scanning a line (11- μm long) RL (green) and LR (red). **j** Distorted flow field obtained by scanning the pattern with x and y broken symmetry and 4.6- μm offset between the forward and reverse paths. **k** Asymmetric flow field obtained by scanning the pattern with x broken symmetry and 4.6- μm offset. **l** Asymmetric flow field obtained by scanning the symmetric pattern **e** and 4.6- μm offset. **m** Symmetric flow field obtained by scanning the symmetric pattern with minimal cost and 4.6- μm offset. Scale bar: 20 μm . LR, left to right; RL, right to left

We speculated that the residual distortion might arise from either the relatively long scanning duration, which prevents the full counteraction of the asymmetries

introduced by the laser movement, or the immediate scanning back and forth of each line, which results in shorter time for the fluid to relax to the ambient

temperature and, hence, in additional perturbations of the flow field. Therefore, we simplified the scan pattern by considering four single-step scan periods $B(x,t) + B(-x,-t) + B(-x,t) + B(x,-t)$ (Fig. 3a): the lines are sequentially scanned (i) LR moving TB, (ii) RL moving BT, (iii) RL moving TB, and (iv) LR moving BT (except for the middle line always scanned RL). Full details are reported in Additional file 1: Table S1 and Additional file 2: Video S1. Nevertheless, the corresponding flow field still displayed a pronounced x -asymmetry explained neither by the long scanning duration nor the insufficient time to reset between the back-and-forth scanning (Fig. 3e).

2.4 Hydrodynamic simulations predict the source of distortions

This residual distortion in the flow field could either be due to an asymmetry in the chamber or an inherent property arising from residual, non-neutralized flow contributions. To distinguish between these two possibilities, we reversed the scanning of the central scan line and found that this results in a mirrored flow field (Additional file 1: Fig. S4a). To understand the origin of this residual asymmetry, we repeated the laser scanning without the central line and we identified a weak, but very apparent, quadrupolar field that would be responsible for this minor asymmetry in the final flow field (Additional file 1: Fig. S4b–e). This problem can be decomposed into two parts: (i) dipolar flow field generated by scanning the middle line twice, and (ii) neutral flow fields generated by scanning the additional lines in a counterdirected manner. However, it is well known that a single line repeatedly scanned in one direction will generate a dipolar flow field [9, 10, 12, 16]. Therefore, we focused our attention on the second possibility.

Interestingly, we found that a single line scanned back and forth gave rise to a quadrupolar field (Fig. 3g), which is predicted by theory only when an offset is included between the forward and reverse paths (Fig. 3h). In fact, the theory predicts no net flow for perfectly aligned lines being scanned back and forth. In addition, including this offset in the symmetric pattern, viz. $B(x,t) + B(-x,-t) + B(-x,t) + B(x,-t)$, the theory predicted a distorted flow field (Fig. 3f) perfectly compatible with the one observed in Fig. 3e. Thus, we deduced that the main contribution to these residual distortions is that of the quadrupolar fields arising from scanning the additional lines in a counterdirected manner.

To generate a neutral flow, the dipolar fields resulting from scanning the lines back and forth have to perfectly overlap to cancel each other. However, the dipoles generated by a single line scanned RL and LR showed tapered lobes, misaligned with the midpoint of the scan path (Fig. 3i). This asymmetry in the dipolar field

could be a result of the elongated, asymmetric shape of the heat spot. We therefore superimposed these mismatched dipolar fields with opposite flow directions and found that it gave rise to a substantial quadrupolar field (Fig. 3g). Thus, we included an offset in the forward and reverse scan paths to compensate for the misalignment of the dipole. A negligible particle displacement was detected by scanning the laser along two counter-directed lines with 4.6- μm offset (Additional file 1: Fig. S4f). Therefore, we included an offset of 4.6 μm between the forward and reverse paths in all the scan patterns (7 parallel lines, 33- μm long and 5.6 μm apart) to cancel any quadrupolar contribution arising from the additional six lines.

Despite these adjustments, the scan patterns with broken symmetries $A(x,t)$ (Fig. 3j) and $A(x,t) + A(x,-t)$ (Fig. 3k) still showed pronounced asymmetries comparable with those observed without compensating for the dipole mismatch (Fig. 3b and c, respectively) due to the asymmetric line-by-line scanning. Although the pattern $A(x,t) + A(x,-t) + A(-x,t) + A(-x,-t)$ (Fig. 3l) proved to be symmetric in the scanning, it exhibited no substantial differences from the corresponding pattern without any offset, likely owing to its long scanning duration (Fig. 3d). Notably, the symmetric scan pattern with the minimal cost, viz. $B(x,t) + B(-x,-t) + B(-x,t) + B(x,-t)$, showed fully restored symmetries with respect to x and y as mirror axes (Fig. 3m). Hence, our approach involving cooperation between three ingredients—i.e. (i) flows and heating disentanglement, (ii) multi-timescale scan-sequence symmetrization, and (iii) residual high-order field cancellation—makes it possible to homogenize the temperature over the sample without introducing side effects in the flow-field symmetry.

2.5 ISO-FLUCS achieves significant reduction in temperature gradients without loss of flow-induction performance

To determine whether the performance of ISO-FLUCS matches that of traditional FLUCS, we used a single line (33- μm long) scanned RL for FLUCS and the pattern $B(x,t) + B(-x,-t) + B(-x,t) + B(x,-t)$ (7 parallel lines, 33- μm long, 5.6 μm apart, 4.6- μm offset between the forward and reverse scan paths) as a benchmark for ISO-FLUCS. Figure 4a and e show the corresponding particle trajectories. The near complete suppression of quadrupolar contributions in the ISO-FLUCS scheme yielded a field symmetry satisfactorily comparable to the dipolar field generated by the single line. Additionally, we measured the velocity of particles travelling along the middle line (highlighted in pink). The corresponding histograms (Fig. 4b and f, respectively) reveal a lower average velocity

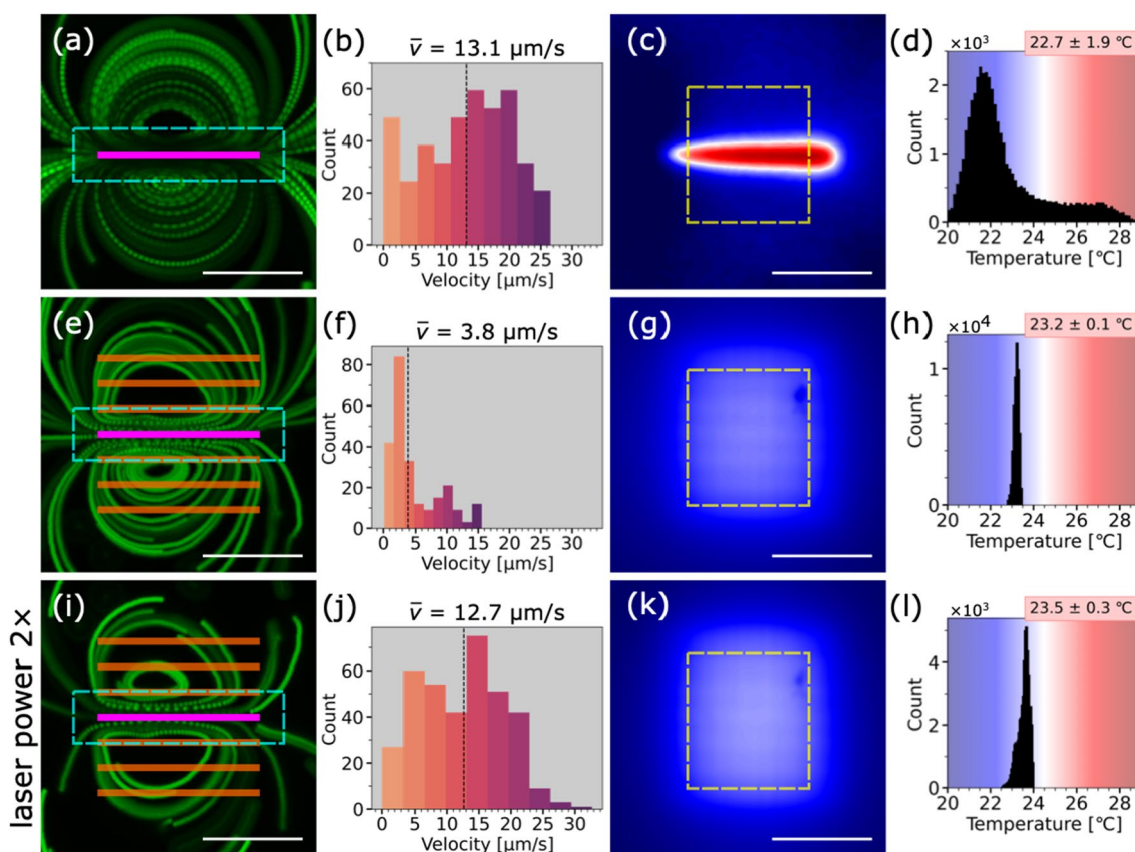


Fig. 4 ISO-FLUCS reduces the temperature impact while still inducing net thermoviscous flows. **a, e** Maximum intensity projection over time showing the particle trajectories obtained by repeated scanning along a single line (**a**, highlighted in pink) and along seven parallel lines (**e**, the lines highlighted in orange are directionally counteracted, while the middle line in pink is always scanned right to left). **b, f** Histograms of the particle velocity measured within the cyan dashed regions highlighted in panels **a** and **e**, respectively, by the TrackMate plugin implemented in the Fiji software. **c, g** Temperature distributions measured from Rhodamine B dispersed in glycerol/water solution by using the scan patterns in **a** and **e**, respectively. **d, h** Corresponding histograms of the temperature measured within the yellow dashed region. **i–l** Particle trajectories, histogram of the particle velocity, temperature distribution, and histogram of the temperature, respectively, measured with the ISO-FLUCS pattern shown in panel **e** by doubling the laser power. Scale bar: 20 μm

in the ISO-FLUCS scheme due to the lower amount of energy locally deposited along each scan line when time-averaged. The particles are ~ 3.4 times slower on average. However, the particle velocity can be easily varied by tuning the laser power or the scan frequency on demand.

The main advantage of using the ISO-FLUCS pattern is clearly evidenced when measuring the temperature distribution over the sample. To this end, we evaluated the time-averaged fluorescence intensity experienced by Rhodamine B in both configurations by keeping the environmental background at 21 $^{\circ}\text{C}$ with a Peltier cooling system. While the repeated laser scanning along a single line gave rise to a strong temperature gradient with a sharp temperature increase from 21 $^{\circ}\text{C}$ up to 29 $^{\circ}\text{C}$ and SD of 1.9 $^{\circ}\text{C}$ (Fig. 4c, d), the ISO-FLUCS pattern produced a more even temperature distribution over the ROI ($25 \times 28 \mu\text{m}^2$) with SD of only 0.1 $^{\circ}\text{C}$ (Fig. 4g, h). In cases where thermoviscous manipulations involve larger

samples, longer and/or additional scan lines should be included in the ISO-FLUCS pattern to cover the entire ROI.

Since the bead velocity scales with ΔT^2 [9, 10] and the temperature T increases linearly with the energy released along the scan path, it is possible to hone our ISO-FLUCS strategy to approach similar flow magnitude achievable by traditional FLUCS. Indeed, a comparable average velocity of 13 $\mu\text{m/s}$ was reached with the ISO-FLUCS pattern by doubling the laser power (Fig. 4i, j). However, it entailed a slight broadening of the temperature distribution with a higher SD of 0.3 $^{\circ}\text{C}$ (Fig. 4k, l).

For completeness, we compared the temperature SD and flow velocities in FLUCS and ISO-FLUCS configurations by keeping constant the absorbed energy per line. The single line in traditional FLUCS was scanned at a laser power of 89 mW obtaining an average flow velocity

of 1.6 $\mu\text{m/s}$ and a temperature SD of 0.9 $^\circ\text{C}$ (Additional file 1: Fig. S5a, b), whereas the ISO-FLUCS pattern scanned at a laser power of 622 mW yielded an average velocity of 7.1 $\mu\text{m/s}$ with a temperature SD of 0.2 $^\circ\text{C}$ (Additional file 1: Fig. S5c, d).

The effective disentanglement between flow field and temperature field achieved by implementing the proposed multi-scanning strategy enables one to change the background temperature on-demand without altering the flow field. Additional file 1: Fig. S6 shows the flow fields obtained with the ISO-FLUCS pattern $B(x,t) + B(-x,-t) + B(-x,t) + B(x,-t)$ at a background temperature of 25 $^\circ\text{C}$, 30 $^\circ\text{C}$ and 35 $^\circ\text{C}$.

2.6 ISO-FLUCS properties are retained in more complex scan patterns

As proof of concept, we demonstrated the ability to precisely transport particles at low temperature impact along arbitrary paths of increased complexity: hexagon (Fig. 5a, c), star (Fig. 5d, f), S-shape (Fig. 5g, i), circle (Fig. 5j, l), spiral (Fig. 5m, o), and ellipse (Fig. 5p, r). These patterns can be classified into two distinct categories: (i)

closed paths (hexagon, star, circle, ellipse), and (ii) open paths (S-shaped, spiral).

The ISO-FLUCS patterns of closed paths consisted of additional concentric shapes equally distributed in the inner and outer sides. To balance the heat accumulation on the inner side of the shapes due to superimposition of denser temperature Gaussian profiles, we gradually increased the spacing between the shapes on approaching the innermost region. With regards to the open patterns, additional S-shaped lines were included in the scan sequence so as to account for the offset and retrace the original track (5.6- μm offset), whereas no additional path was needed for the spiral since the winding was conveniently selected to inherently minimize the temperature gradient. Full details on the pattern geometry and scan sequence are reported in Additional file 1: Table S1 and Additional file 3: Video S2.

The temperature measurement with Rhodamine B (background maintained at 21 $^\circ\text{C}$ using a Peltier cooling system) revealed that all the explored ISO-FLUCS patterns (hexagon Fig. 5b, star Fig. 5e, S-shape Fig. 5h, circle Fig. 5k, spiral Fig. 5n, and ellipse Fig. 5q) yielded

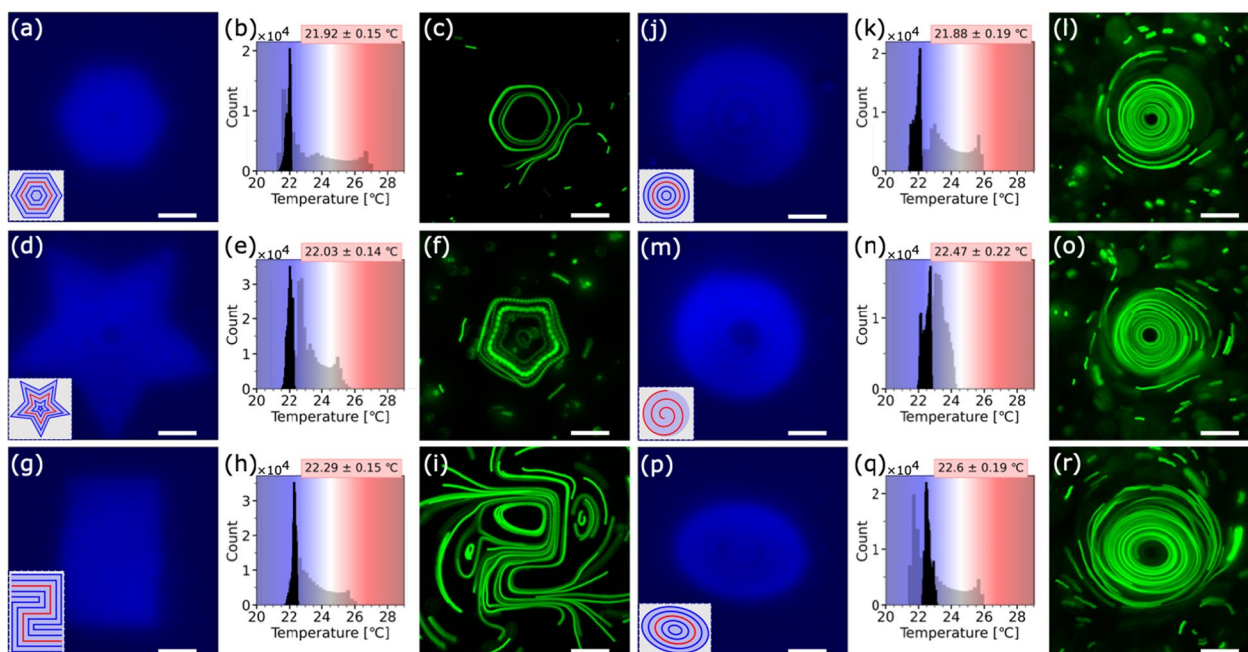


Fig. 5 Special solutions for patterns of increased complexity. Temperature distributions, corresponding temperature histograms, and particle trajectories yielded by the repeated scanning along **a–c** five concentric hexagons, **d–f** five concentric star-shaped paths, **g–i** five S-shaped lines, **j–l** five concentric circles, **m–o** a spiral, and **p–r** five concentric ellipses, respectively. The bottom-left insets in panels **a, d, g, j, m, p** show the patterns scanned by the laser beam. Blue and red lines were used to distinguish between counteracted and non-counteracted scan paths, respectively. Specifically, in panels **a, d, j, p** the shapes were scanned clockwise from the outermost to the innermost region in the first period, and counterclockwise from the innermost to the outermost region in the second period (except for the middle one that was scanned twice counterclockwise). In panel **g**, the lines are scanned starting from top-left and following the shape in the first period, while from bottom-right in the second period (except for the middle path which was scanned twice starting from bottom-right). In panel **m**, the spiral is scanned counterclockwise from outside to inside. The shaded histograms in panels **b, e, h, k, n, q** represent the temperature distributions measured by using the corresponding FLUCS patterns (see also Additional file 1: Fig. S7). Scale bar: 20 μm

a significantly narrower temperature distribution (up to 11.3 times) compared to the one obtained with the FLUCS pattern (shaded histograms in Fig. 5b, e, h, k, n, q and Additional file 1: Fig. S7). Hence, case-specific, tailored solutions consisting of series of scan lines with near isothermal temperature distributions can be conceived even when more complex scan patterns are considered.

2.7 In vivo manipulation of *C. elegans* cytoplasm

To further evaluate the superiority of ISO-FLUCS over FLUCS in living biological systems we used it for in vivo manipulation of *C. elegans* embryos. We firstly created a simple and predictable environment whose geometry and background temperature were compatible with those needed for handling worm embryos. Given their elliptical shape with a minor axis of approximately 25–30 μm , we built a chamber of thickness 20 μm capable of housing and immobilizing developing embryos without destructively compressing them. The background temperature was kept at physiological conditions of 15 $^{\circ}\text{C}$ using a Peltier cooling system.

In an effort to arbitrarily rotate the cytoplasm, we designed elliptical scan paths whose geometry could be dynamically tuned to fit the embryo shape. For preliminary testing in the controlled environment, we used a FLUCS pattern comprising a single ellipse of 40/28 μm major/minor axis and an ISO-FLUCS pattern of concentric ellipses. To further improve the temperature homogeneity, we adopted two alternating ISO-FLUCS patterns (switching time 0.5 s) whose ellipses were conveniently offset to flatten the ripples still visible in Fig. 5p. Additionally, we scanned all the ellipses counterclockwise to enhance the cytoplasm rotation. Full details of the pattern geometry and scan sequence are reported in Additional file 1: Table S1 and Additional file 3: Video S2.

The FLUCS pattern gave rise to a wide temperature distribution with SD of 2.0 $^{\circ}\text{C}$ (Fig. 6a, b). The absolute temperature rose up to 22.3 $^{\circ}\text{C}$ (+7.3 $^{\circ}\text{C}$ above the background) rendering it unsuitable for investigating homeothermic systems. In contrast, the ISO-FLUCS pattern produced a much more uniform temperature rise with SD of 0.13 $^{\circ}\text{C}$ (15 times lower) and a temperature peak of 16.6 $^{\circ}\text{C}$ (+1.6 $^{\circ}\text{C}$ above the background) (Fig. 6e, f). Additionally, we evaluated the flow trajectories and the particle velocities in a highly viscous medium (pure honey) and found that there was no substantial difference to the flow profile and speed when moving from the FLUCS (Fig. 6c, d) to the ISO-FLUCS pattern (Fig. 6g, h): the average velocities were 13.2 $\mu\text{m}/\text{s}$ and 12.0 $\mu\text{m}/\text{s}$, respectively.

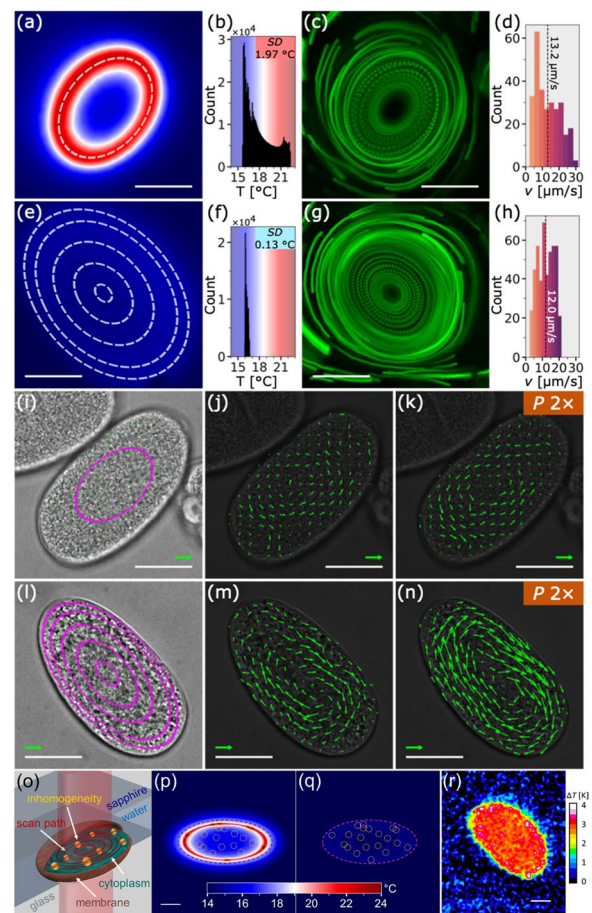


Fig. 6 ISO-FLUCS induces in vivo intracellular streaming in *C. elegans* with even temperature distribution. **a, e** Temperature distributions, **b, f** temperature histograms, **c, g** particle trajectories, and **d, h** histograms of the particle velocity yielded by repeatedly scanning the laser counterclockwise along a single ellipse and concentric ellipses, respectively (white dashed ellipses highlighted in panels **a** and **e**). **i, l** Endogenous flows in early-stage developing *C. elegans* embryos in the absence of external stimuli. The laser was scanned along the patterns highlighted in magenta. **j, k, m, n** Cytoplasmic streaming obtained by scanning along a single ellipse clockwise and along concentric ellipses counterclockwise, respectively (in panels **k, n** the laser power was doubled) (Additional file 4: Video S3). To improve clarity, the brightness in panels **j, k, m, n** was reduced and the four alternating ellipses in panels **e** and **l** were omitted (see Additional file 1: Table S1 and Additional file 3: Video S2 for more details). Scale bar: 20 μm . Flow field unit bar (green arrow): 0.5 $\mu\text{m}/\text{s}$. **o** Rendering of the simulation model implemented in COMSOL Multiphysics. **p, q** Steady-state solution of the temperature distributions obtained by scanning along a single ellipse and five concentric ellipses, respectively. The dashed pink lines in panels **p, q**, highlight the cross section of the embryo membrane, whereas the dotted yellow circles in panels **p, q** represent the cross section of the protein domains. Scale bar: 10 μm . **r** mCherry differential intensity measurement indicating an even temperature distribution inside a *C. elegans* embryo during ISO-FLUCS. Scale bar: 10 μm

Finally, we demonstrated that these fields are able to generate and control flows in worm embryos well in excess of endogenous streaming. Figure 6i, l shows two representative early-stage embryos in which the endogenous flows are negligible and comparable on the time scale of seconds (Additional file 1: Fig. S8). The laser scanning along the elliptical patterns (highlighted in magenta) gave rise to a directional rotation of the cytoplasm, whose magnitude visibly increased when the laser power was increased (Fig. 6j, k, m, n, Additional file 4: Video S3 and Additional file 5: Video S4). An enhanced rotational speed of the cytoplasm was observed by using the ISO-FLUCS pattern (Fig. 6m, n) compared to the FLUCS pattern (Fig. 6j, k) thanks to the coherent scanning direction (all the concentric ellipses were scanned CCW, see Additional file 1: Table S1 and Additional file 3: Video S2).

We eventually tested the ISO-FLUCS patterns in developing *C. elegans* embryos to consolidate the reduced invasiveness of this technique as already demonstrated in previous studies by using conventional FLUCS pattern [12, 13]. In this work, we even further minimized the risk that we altered the natural course of development: the embryos continued unaffectedly their progression towards division up to at least first cleavage (Additional file 6: Video S5 and Additional file 7: Video S6).

It was previously established in simulations that the assumption of a homogeneously heat conducting, water dominated cytoplasm is sufficient to explain temperature profiles carefully mapped by life-time imaging of nitrogen vacancies in nanodiamonds [26]. As intra-cellular temperature measurements have historically been subject to heated debates, we decided to adapt the simulations for ISO-FLUCS and specifically study their robustness versus deviation in the thermal conductivity of the cytoplasm. For this we made use of established literature values for tissues and their constituents. Specifically, to infer the laser-induced heating in *C. elegans* embryos, we designed an embryo model in COMSOL Multiphysics to solve the heat-conduction equation (Fick's law). An illustration of the simulation domain with a cytoplasm with a thermal conductivity of $0.54 \text{ W m}^{-1} \text{ K}^{-1}$ (assuming about 20% protein content, [27]) and poorly heat conducting large inhomogeneities ($0.27 \text{ W m}^{-1} \text{ K}^{-1}$ corresponding to pure protein [27]) as well as phospholipid membrane ($0.2 \text{ W m}^{-1} \text{ K}^{-1}$, [28]) is depicted in Fig. 6o. Figure 6p, q show the steady-state solutions of the temperature distribution evaluated in the plane $z = 0$ for FLUCS and ISO-FLUCS, respectively. While FLUCS gave rise to a relatively wide temperature range with a SD of $2.7 \text{ }^\circ\text{C}$, the ISO-FLUCS pattern consisting of five concentric ellipses (see Additional file 1: Table S1 for more details) produced a much more homogenous temperature distribution. No

strong difference in the temperature distribution was observed when considering the embryo as a plain water-based ellipsoid (no protein domains and phospholipid membrane) (Additional file 1: Fig. S9), which confirms the earlier view that heat conductance is dominated by the water-rich cytoplasm and even robust against hypothetical inhomogeneities. Further simulations reveal reasonable robustness of laser-induced temperature distributions even with extreme variation, like a $30 \text{ }\mu\text{m}$ elongated needle with $3 \text{ }\mu\text{m}$ diameter and a thermal conductivity of stainless steel embedded in the cytoplasm (Additional file 1: Fig. S10).

This strongly suggests that the temperature distribution inside the embryo is likely dominated by the choice of the scan pattern and likely not by the local deviation of the thermal conductivity from water-based cytosol. This is suggesting that in particular, ISO-FLUCS should yield homogenous temperature distributions also in the actual embryos.

In order to show this, we adopted temperature measurements with the temperature sensitive protein fluorophore mCherry [29], in our case bound to the histone H2B, which at earliest stages of development is present also inside the cytoplasm of the embryo. Applying the same ISO-FLUCS pattern again, we found that indeed that ISO-FLUCS yields homogenous temperature distributions also in vivo (Fig. 6r).

On the other hand, the normal FLUCS stimulus yielded a strong temperature gradient across the embryo, in good absolute agreement with in vitro measurements (Additional file 1: Fig S10c, d). Even though the differential nature of these measurements in the presence of photobleaching inherently limits signal-to-noise, both relative temperature distribution and good agreement on an absolute scale clearly support theoretical arguments and simulations.

Our findings not only reinforce the reduced invasiveness of IR-driven thermoviscous flows, but also confirm the validity of ISO-FLUCS as the new non-invasive standard for this type of optical micromanipulation.

3 Conclusions and outlook

Here, we show that ISO-FLUCS can drastically improve the temperature homogeneity inside samples (SD reduced up to 20 times) while retaining the positive features of FLUCS (i.e., contact- and probe-free, physiological, directed, haptic, sub-micrometric control and predictable flow field with velocities up to tens of $\mu\text{m/s}$). These remarkable results were achieved by implementing three new ingredients to the well-established FLUCS: (i) flow and heating disentanglement, (ii) multi-timescale scan sequence symmetrization, and (iii) residual high-order field cancellation. Specifically, neutral scan lines

were conveniently included in the pattern to flatten the temperature gradient in the most sensitive region (hundreds of μm^2). Then, spatiotemporally symmetric scan sequences ensured predictable and highly symmetric thermoviscous flow fields.

Although the heating level in conventional FLUCS was previously demonstrated to be tolerable in sensitive biological systems, such as developing *C. elegans* zygotes [12, 13], more fragile samples, such as homothermic mammalian embryos, may require greater temperature stability and homogeneity.

Concrete examples of beneficial applications for ISO-FLUCS include (i) the study of phase-separated condensates within biological cells which can be temperature sensitive [30, 31], and yet would be desirable to manipulate by flows. (ii) Localized temperature stimuli are known to be able to affect cell-division timing [26], which can be prevented by ISO-FLUCS, and (iii) intracellular and intranuclear rheology through optical manipulation can also benefit from even laser-induced heating since the mechanical properties of materials may be susceptible to temperature changes [12, 13, 32]. The strongly reduced invasiveness offered by ISO-FLUCS may contribute to advancing the awareness of the physical mechanisms governing temperature sensitive systems such as (iv) nuclear mechanics [33] and chromatin organization [34]. (v) Controlled temperature manipulation with ISO-FLUCS might be also leveraged at subcellular to maintain control over temperature-sensitive proteins [29] such as during cortical flow manipulations, and the disentanglement of flows and heating, is a powerful way to separate flow induced effects from thermophoresis [35]. Moreover, ISO-FLUCS offers the possibility to (vi) control the conformation of thermoresponsive polymers [36, 37], (vii) prevent undesired local changes when in standardized biochemical assays with temperature sensitive buffers such as TRIS for PCR, (viii) prevent thermotaxis of micro-organism during flow manipulations, (ix) improve sensitive quantitative imaging assays, as many dyes are temperature dependent, and finally (x) pave the way to flow manipulations of temperature sensitive mammalian embryos, a pre-requisite to any clinical application.

Moreover and more generally, this work serves to extend applications to sensitive biological samples and the study of rheological properties of phase-separated condensates, the likely strongest contemporary field of cell biology, towards which we will contribute in aspects relating to temperature [30, 38–41]. Since biochemical networks usually react on time scales of seconds to hours [42], ISO-FLUCS, whose typical time scale is milliseconds, would not result in any side effects to the sample, such as temperature-related stress. Thus, considering the

measured *SD* of only $0.1\text{ }^\circ\text{C}$ in contrast to the *SD* of $1.9\text{ }^\circ\text{C}$ exhibited by FLUCS, we expect ISO-FLUCS to drastically reduce the temperature stress in the sample and, hence, to safely extend the capabilities of the technique to some of the most delicate systems.

The clean disentanglement of flows and local heating that ISO-FLUCS offers will not only become the new unimpeachable standard for precise flow manipulation inside a living specimen. It additionally lays the foundations to specifically address different classes of physical stimuli, relating to mechanics and forces on one hand, and temperature-dependent biochemistry of rate equations on the other. As an example, this will advance flow-driven microrheology, by eliminating any temperature-dependent material responses caused by the measurements. Additionally, as ISO-FLUCS operates over an ultra-narrow temperature range, it is also expected to find wide use in studying temperature-sensitive polymeric or particulate hydrogels, where the accurate determination of the sol–gel transition is of utmost importance for understanding emerging properties on the macroscale [43–45]. The fine temperature control in ISO-FLUCS can be also used to investigate the spinodal decomposition of many systems that exhibit high propensity towards phase-separation [46, 47].

For these reasons, we believe that ISO-FLUCS will replace FLUCS in becoming the new standard for such laser-induced optical micromanipulations. Additionally, ISO-FLUCS resonates with a rapidly growing community to harness the power of temperature stimuli in manipulating colloidal and living systems on the micro- and nanoscale [5, 6, 48–52]. In the medium-term future, we foresee ISO-FLUCS paving the way to medical use cases, e.g. in the field of laser-assisted human reproductive medicine.

4 Materials and methods

4.1 Optical layout capable of simultaneous imaging and generating thermoviscous flows

The experiments we reported herein were performed using the FLUCS technology described in detail by Mitasch et al. [12]. Briefly, simultaneous generation and observation of thermoviscous flows was achieved by coupling a fiber-based infrared Raman laser (1455 nm wavelength, 20 W maximum power, continuous-wave mode, CRFL-20-1455-OM1, Keopsys) to the beam path of an Olympus IXplore microscope through a dichroic mirror (DM2:DMSP805, Thorlabs) (Fig. 1a). An acousto-optic deflector (two-axis AOD, AA.DTSXY-A6-145, Pegasus Optik) and a custom-coated 60× objective lens (UPLSAPO, NA = 1.20, W-IR coating, Olympus) were used to dynamically deflect and focus the laser beam in

the microscope focal plane, respectively. While infrared absorption of the medium creates temperature gradients within the sample, Peltier elements attached to a highly thermally conductive sapphire slide control the absolute temperature of the whole sample.

In the experiments a laser power of 470 mW was used where not otherwise specified. For experiments in *C. elegans* embryos, laser powers of 288 mW and 576 mW were used. The laser powers reported in the work refer to those measured before injecting the laser beam into the optical path. The actual power that reaches the sample was estimated to be 5–10 times lower.

4.2 Fluorescence-based temperature measurement

The time-averaged temperature distribution was inferred from measuring the fluorescence intensity of 0.02% Rhodamine B dye (0.2% in isopropanol, 02558-100ML, Sigma-Aldrich) in glycerol/water (1:1) solution. The fluorescence intensity is linearly related to the temperature change with the proportionality constant $-0.0074/\text{K}$ (Additional file 1: Fig. S1). The ROI size was $25 \times 28 \mu\text{m}^2$ in the case of seven parallel lines, whereas it covered the whole pattern extent in the case of special ISO-FLUCS patterns in Fig. 5. Fluorescence images were blurred with 500-nm radius Gaussian filter to eliminate the high-frequency noise—the temperature profile decayed within approximately $5 \mu\text{m}$ (Fig. 2a, b).

To minimize the impact of photobleaching, we averaged the dye intensity over periods of 5.4 s before and after switching on the IR laser. We found the intensity drop due to the dye photobleaching resulted to be negligible on this time scale: only $0.005 \text{ }^\circ\text{C}$ (see Additional file 1: Fig. S11 for more details). Additionally, we switched off the excitation light for 2 min between each set of measurements to allow the dye to recover.

The influence of thermophoresis was minimized by periodically exposing the sample to the heating stimuli and using only the fluorescence images acquired shortly after the laser exposure. The reduction in quantum yield experienced by the dye occurs on a much shorter time-scale than thermophoresis. However, a slight asymmetry of the temperature distribution along the scan line is visible in Fig. 4c, which can be attributed to thermophoresis. To further suppress the contribution of thermophoresis, the dye molecules could be immobilized in place, for instance by covalently linking them to a matrix gel.

To reliably control the absolute temperature during the laser scanning, the sample was embedded between a borosilicate glass coverslip (22-mm diameter, 0.17-mm thickness, VWR) and a high thermally conductive sapphire slide (thermal conductivity = $27.1 \text{ W m}^{-1} \text{ K}^{-1}$, model SMS-7521, UQG Optics). The sapphire slide was actively cooled using proportional-integral-derivative

controlled Peltier elements (model TES1-127021, TEC, Conrad).

4.3 Heuristic simulations

The heuristic approach we adopted to infer information about the scan pattern that minimized the temperature gradient within the ROI consisted of four steps:

1. Quantitative measurement of the time-averaged temperature gradient due to the laser exposure. The fluorescence intensity of Rhodamine B was measured across the scanned region (Fig. 2a, b) and the absolute temperature was evaluated by referring to the calibration curve in Additional file 1: Fig. S1.
2. Semi-empirical simulation of the temperature distribution induced by two heating spots as a function of their separation distance (Fig. 2e). The final distribution was obtained by summing two Cauchy-Lorentz temperature profiles as inferred in step (1):

$$T(x, y) = T_1(x, y) + T_2(x, y). \quad (2)$$

Then, the *SD* of the temperature distribution was evaluated across the junction between the spots and the optimal distance ensuring the highest temperature homogeneity was inferred by plotting the *SD* as a function of the separation distance (Fig. 2f).

3. Semi-empirical simulation of the temperature distribution induced by a given scan path. The path was firstly discretized into N points with a spatial step of $5.6 \mu\text{m}$ (this value corresponded to the actual scan step). The final distribution was obtained by summing the temperature profile of the N heating spots as inferred in step (1):

$$T(x, y) = \sum_{i=1}^N T_i(x, y). \quad (3)$$

Additional heating spots ($5.6\text{-}\mu\text{m}$ lattice period) were iteratively patterned in order to homogenize the temperature in the ROI. Specifically, the script was initialized by randomly placing a single point at a distance of $5.6 \pm 0.1 \mu\text{m}$ from the given scan path. Then, additional points (x_i, y_i) were sequentially placed in the ROI with minimal spatial cost (point-to-point distance kept at $5.6 \mu\text{m}$) up to a complete covering of the ROI:

$$(x_i, y_i) = \min_{(x_i, y_i) \in \text{ROI}} \left\{ \sum_{j=1}^{N+m} \sqrt{(x_i - x_j)^2 + (y_i - y_j)^2} \right\}, \quad (4)$$

where (x_j, y_j) are the coordinates of all the points already present in the ROI (i.e. N points in which the scan path was discretized plus m new points

iteratively appended to the lattice). Eventually, the SD of the temperature distribution in the ROI was evaluated over a large number of generated lattices (randomly initialized) and the lattice corresponding to the minimal SD was considered (Fig. 2g).

4. Scan path outlining with minimal cost. The additional heating points were clustered according to their distance from the given scan path (Additional file 1: Fig. S3).

4.4 Scan pattern design

To generate thermoviscous flows with an even temperature distribution over large areas (hundreds of μm^2), we included neutral flow scan lines in the pattern in order to flatten the local heating without interfering with the desired flow direction. The ISO-FLUCS patterns and the corresponding scan sequences adopted in this work are summarized in Additional file 1: Table S1, Additional file 2: Video S1 and Additional file 3: Video S2. All the FLUCS and ISO-FLUCS patterns adopted in the current work are scanned at 2000 Hz.

4.5 Sample preparation for stream visualization

To visualize the flow fields, we traced over time fluorescent polystyrene microspheres embedded in a highly viscous medium (pure honey). Specifically, 0.5 μL of Dragon Green-labelled polystyrene microspheres ($\lambda_{\text{exc}} = 480 \text{ nm}$, $\lambda_{\text{em}} = 520 \text{ nm}$, 1- μm diameter, PS-COOH•, 1.05% solids, FC04F, Bangs Laboratories Inc.) and 0.1 μL of plain polystyrene micro-spacers (5- μm diameter, P(S/2% DVB), 9.9% solids, PS06N, Bangs Laboratories Inc.) were dispersed in 16 μL of pure honey. A volume of 3 μL was dropped on a microscope slide and gently covered with a borosilicate glass coverslip (22-mm diameter, 0.17-mm thickness, VWR). The chamber was sealed with dental impression material (Identium Light Fast, Kettenbach dental). TrackMate plugin implemented in the Fiji software [53] was used to track particles and to measure their velocity.

4.6 Mounting of *C. elegans* embryos

Caenorhabditis elegans wildtype strain N2 was kept and cultured at 16 °C on standard feeding plates. Prior to measurement, one adult worm was dissected in 10 μL of buffer M9 on a \varnothing 18-mm No. 1.5H cover glass (Marienfeld, cat. no. 0117580). Polystyrene spacer beads of a diameter of 20 μm (Polyscience, cat. no. 18329) were added to a final concentration of around 0.08% (w/v) to control the chamber height. The cover glass was mounted onto a 1-mm thick sapphire glass of a custom-made temperature stage such that the preparation containing

the embryos of various developmental stages was sandwiched between the cover glass and the temperature stage, as previously described [12]. The advantages of placing the embryos into a chamber lie in the reduction of motion/drift and in the achievement of a sufficient focus of the laser beam, while the restriction does not interfere with the well-being of the embryo. Such chambers are well established for the work with *C. elegans* embryos [54].

During the flow manipulation experiments inside the embryos, the microscope stage was actively cooled from an ambient temperature of 18 °C to 15 °C using proportional-integral-derivative (PID) controlled Peltier elements (TES1-127021, TEC, Conrad). For experiments, one-cell *C. elegans* embryos were used. Flow velocities induced in *C. elegans* embryos were quantified using PIVlab [55], a digital particle image velocimetry (PIV) tool implemented in MATLAB.

Measurement of the temperature distribution in *C. elegans* embryos were performed by evaluating the fluorescence intensity reduction of mCherry dyes (labelling histone H2B proteins [56]) during the laser scanning (see Section S1 in Supplementary for more details).

4.7 Hydrodynamic simulations

In our hydrodynamic simulations, we used the theoretical model of FLUCS presented in detail by Liao et al. [10] and extended it to scan patterns involving multiple scan paths, as in ISO-FLUCS. Specifically, a viscous fluid was confined between rigid parallel plates at $z = 0$ and $z = h$, and a heat spot translated along a single, finite scan path, from $x = -l$ to $x = l$ along the line $y = 0$. The instantaneous temperature field of the fluid $T(x, y, z, t)$ during one scan could be written as $T(x, y, z, t) = T_0 + \Delta T(x, y, z, t)$, where T_0 is the reference temperature and $\Delta T(x, y, z, t)$ is the instantaneous, local temperature change due to the laser. The temperature change is modelled as a Gaussian, given by:

$$\Delta T(x, y, t) = \Delta T_0 A(t) e^{-\frac{(x-Ut)^2 + y^2}{2a^2}}, \quad (5)$$

where ΔT_0 is the peak temperature change, a is the characteristic radius, U is the (constant) speed of translation of the heat spot, and $A(t)$ is its dimensionless, time-dependent amplitude. This is valid during one scan, i.e. for $-l/U \leq t \leq l/U$. The choice of a Gaussian temperature profile is motivated by experimental measurements [9, 12]. It allows an analytical solution for the flow field, while capturing the key physics of net flow generation [10].

The heat spot causes a small change in the density ρ and the viscosity η of the fluid locally, via the linear relationships:

$$\rho = \rho_0(1 - \alpha \Delta T), \tag{6}$$

$$\eta = \eta_0(1 - \beta \Delta T), \tag{7}$$

respectively, where ρ_0 and η_0 are the reference density and viscosity, respectively, of the fluid at temperature T_0 , α is the thermal expansion coefficient and β is the thermal viscosity coefficient. This drives an inertialess fluid flow, which in turn causes net displacement of tracers in the fluid.

In the limit $\alpha \Delta T_0, \beta \Delta T_0 \ll 1$, the problem could be solved analytically for the leading-order net displacement of tracers in the fluid with any initial position $\mathbf{X}_0 \equiv (X_0, Y_0)$ due to one scan of the heat spot along the scan path. This is given by:

$$\Delta \mathbf{X}(\mathbf{X}_0) = \alpha \beta \Delta T_0^2 \int_{-t_0}^{t_0} \mathbf{u}_{1,1}(\mathbf{X}_0, t) dt, \tag{8}$$

where $t_0 \equiv l/U$ is half the scan period and $\mathbf{u}_{1,1}$ is the instantaneous fluid velocity field at order $\alpha \beta$. The instantaneous flow field $\mathbf{u}_{1,1}$ during one scan is given by:

$$\begin{aligned} \mathbf{u}_{1,1}(\mathbf{x}, t) = A(t)^2 U & \left\{ \mathbf{e}_x \left[\frac{a^2}{4r^2} - \frac{a^2(x-Ut)^2}{2r^4} + \left[-\frac{a^2}{2r^2} + \frac{a^2(x-Ut)^2}{r^4} \right] e^{-r^2/2a^2} \right. \right. \\ & + \left. \left[\frac{a^2}{4r^2} - \frac{a^2(x-Ut)^2}{2r^4} \right] e^{-r^2/a^2} - \frac{1}{4} E_1(r^2/2a^2) + \frac{1}{4} E_1(r^2/a^2) \right. \\ & \left. \left. + \mathbf{e}_y \left[-\frac{a^2(x-Ut)y}{2r^4} + \frac{a^2(x-Ut)y}{r^4} e^{-r^2/2a^2} - \frac{a^2(x-Ut)y}{2r^4} e^{-r^2/a^2} \right] \right\}, \tag{9} \end{aligned}$$

where $r \equiv [(x-Ut)^2 + y^2]^{1/2}$ is the distance to the centre of the heat spot at time t and E_1 is the exponential integral, given by:

$$E_1(z) \equiv \int_z^\infty \frac{e^{-s}}{s} ds. \tag{10}$$

The net displacement due to a scan path at any given position and orientation may then be obtained by translating and rotating the result above for a scan path at the origin.

For our hydrodynamic simulations of ISO-FLUCS experiments, we computed the net displacement of tracers in the fluid due to sequential translation of the laser along multiple scan paths, which form a scan pattern. To leading order, this is simply given by the sum of the net displacements due to each of the scan paths in the scan pattern. The average velocity field of tracers could then be calculated by dividing the net displacement of a tracer (with arbitrary initial position) due to the scan pattern by

the time taken for the full scan pattern. This corresponds to the trajectories of tracers due to repeated scanning of the heat spot, as shown in Fig. 3f and h. The dimensionless speeds indicated by the colorbar have been scaled by $\alpha \beta \Delta T_0^2 U$.

In our simulations, we used $a = 4 \mu\text{m}$. Following previous work [10, 12], we also chose the amplitude of the heat spot to be sinusoidal, given by:

$$A(t) = \cos^2\left(\frac{\pi t}{2t_0}\right) \tag{11}$$

for $-t_0 \leq t \leq t_0$.

4.8 Thermodynamic simulations

To infer the temperature distribution in *C. elegans* embryos, we numerically solved the heat-conduction equation (Fick's law) under local laser stimuli by using the finite element method (FEM) in COMSOL Multiphysics. The simulation framework consisted of an embryo-like ellipsoid ($a_x = 25 \mu\text{m}$, $a_y = 15 \mu\text{m}$, $a_z = 10 \mu\text{m}$) surrounded by a water layer of thickness $20 \mu\text{m}$, the lat-

ter being sandwiched between a sapphire slide ($170 \mu\text{m}$ thickness) and a glass slide (1mm thickness). To emulate the embryo environment, we defined a medium with a thermal conductivity (κ) of $0.54 \text{W m}^{-1} \text{K}^{-1}$ as cytoplasm, a thin layer (10nm thickness) with $\kappa = 0.20 \text{W m}^{-1} \text{K}^{-1}$ as phospholipid membrane [28], and randomly distributed spheres ($4\text{--}5 \mu\text{m}$ diameter) with $\kappa = 0.27 \text{W m}^{-1} \text{K}^{-1}$ as protein domains [27]. The temperature of the glass slide was set at $15 \text{ }^\circ\text{C}$ to emulate the cooling stage, whereas the remaining domains/interfaces could freely transfer the heating. The rendering of the simulation workspace is shown in Fig. 6o. The meshing was adaptive and chosen to be finer close to the embryo.

Supplementary Information

The online version contains supplementary material available at <https://doi.org/10.1186/s43593-023-00049-z>.

Additional file 1: Figure S1. Temperature measurements in Rhodamine B chamber. **Figure S2.** Time-resolved fluorescence-temperature measurements. **Figure S3.** Heuristic simulation to design ISO-FLUCS

patterns. **Figure S4.** Residual flow fields arising from fully counteracted scan patterns. **Figure S5.** Temperature *SD* and flow velocities at the same absorbed energy per line. **Figure S6.** Temperature distributions and flow fields at different background temperatures. **Figure S7.** Temperature fields induced by FLUCS patterns of increased complexity. **Figure S8.** Physiological state of early-stage *C. elegans* embryos prior to laser exposure. **Figure S9.** Simulated laser-induced heating in presence of a highly conductive material. **Figure S10.** Laser induced heating distributions in *C. elegans*. **Figure S11.** Quantification of the photobleaching rate of Rhodamine B dye. **Section S1.** Fluorescence-based temperature measurement in *C. elegans* embryos. **Table S1.** Geometrical parameters and sequence order of the ISO-FLUCS patterns.

Additional file 2: Video S1. Animation of the laser scanning of ISO-FLUCS patterns A and B.

Additional file 3: Video S2. Animation of the laser scanning of ISO-FLUCS patterns of increased complexity.

Additional file 4: Video S3. FLUCS vs ISO-FLUCS in *C. elegans*.

Additional file 5: Video S4. ISO-FLUCS in *C. elegans* at different laser power.

Additional file 6: Video S5. ISO-FLUCS during embryo mitosis.

Additional file 7: Video S6. ISO-FLUCS with directionally oscillating patterns during embryo mitosis.

Acknowledgements

We thank Iain Patten for valuable discussions on the structure and layout of the manuscript, and Matthäus Mittasch, Anatol Fritsch and Matthias Loidolt for the construction of the microscope and early experiments. Moreover, we acknowledge the support of the Karlsruhe School of Optics & Photonics (KSOP) financed by the Ministry of Science, Research and the Arts of Baden-Württemberg as part of the sustainability financing of the projects of the Excellence Initiative II.

Author contributions

AM and MK conceived the experiments. AM collected the data, and AM and MK analyzed it. SW provided technical support with handling the biological samples and contributed to the data acquisition. EE implemented the software control used in the data acquisition. EE and IDS provided technical support with operating the setup and contributed to the data acquisition and analysis of the flow field profile and temperature distribution. WL and EL performed hydrodynamic simulations to support the experimental results. MK supervised the project. AM and MK wrote the manuscript. All authors contributed to revisions of the manuscript. All authors read and approved the final manuscript.

Funding

We acknowledge funding by the Max Planck Society, the Karlsruhe Institute of Technology. MK further acknowledges support by the European Research Council, in particular the ERC Starting Grant GHOSTs (Grant No. 853619) as well as support by the Volkswagen Foundation (Life! Grant No. 92772), the Max Planck Society, Karlsruhe Institute of Technology, and the Hector Foundation, and funding by the Deutsche Forschungsgemeinschaft (DFG, German Research Foundation) under Germany's Excellence Strategy—2082/1—390761711. WL gratefully acknowledges funding from the Engineering and Physical Sciences Research Council (EPSRC studentship).

Availability of data and materials

Data available from the corresponding author upon reasonable request.

Declarations

Competing interests

MK, EE, and IDS are authors of patents of the FLUCS technology. MK is acting as a consultant for Rapp Opto-Electronic GmbH, Wedel, Germany, that commercialized FLUCS technology.

Author details

¹Max-Planck-Institute of Molecular Cell Biology and Genetics, Dresden, Germany. ²Department of Applied Mathematics and Theoretical Physics, University of Cambridge, Cambridge, UK. ³Center for Systems Biology Dresden, Dresden, Germany. ⁴Institute of Biological and Chemical Systems-Biological Information Processing, Karlsruhe Institute of Technology, Karlsruhe, Germany.

Received: 16 March 2023 Revised: 10 May 2023 Accepted: 24 May 2023

Published online: 18 July 2023

References

1. J. Li, E.H. Hill, L. Lin, Y. Zheng, Optical nanoprinting of colloidal particles and functional structures. *ACS Nano* **13**, 3783–3795 (2019). <https://doi.org/10.1021/acsnano.9b01034>
2. L. Lin, E.H. Hill, X. Peng, Y. Zheng, Optothermal manipulations of colloidal particles and living cells. *Acc. Chem. Res.* **51**, 1465–1474 (2018). <https://doi.org/10.1021/acs.accounts.8b00102>
3. G. Nalupurackal, M. Gunaseelan, S. Roy et al., A hydro-thermophoretic trap for microparticles near a gold-coated substrate. *Soft Matter* (2022). <https://doi.org/10.1039/D2SM00627H>
4. A.N. Koya, J. Cunha, T. Guo et al., Novel plasmonic nanocavities for optical trapping-assisted biosensing applications. *Adv. Opt. Mater.* **8**, 1901481 (2020). <https://doi.org/10.1002/adom.201901481>
5. Y. Liu, H. Ding, J. Li et al., Light-driven single-cell rotational adhesion frequency assay. *e-Light* **2**, 13 (2022). <https://doi.org/10.1186/s43593-022-00020-4>
6. S. Liu, L. Lin, H.-B. Sun, Opto-thermophoretic manipulation. *ACS Nano* **15**, 5925–5943 (2021). <https://doi.org/10.1021/acsnano.0c10427>
7. S. Xie, Y. Du, Y. Zhang et al., Aptamer-based optical manipulation of protein subcellular localization in cells. *Nat. Commun.* **11**, 1347 (2020). <https://doi.org/10.1038/s41467-020-15113-2>
8. M. Kreysing, Probing the functional role of physical motion in development. *Dev. Cell.* **51**, 135–144 (2019). <https://doi.org/10.1016/j.devcel.2019.10.002>
9. F.M. Weinert, D. Braun, Optically driven fluid flow along arbitrary micro-scale patterns using thermoviscous expansion. *J. Appl. Phys.* **104**, 104701 (2008). <https://doi.org/10.1063/1.3026526>
10. W. Liao, E. Erben, M. Kreysing, E. Lauga, Theoretical model of confined thermoviscous flows for artificial cytoplasmic streaming. *Phys. Rev. Fluids* **8**, 034202 (2023). <https://doi.org/10.1103/PhysRevFluids.8.034202>
11. N.T. Chartier, A. Mukherjee, J. Pfanzelt et al., A hydraulic instability drives the cell death decision in the nematode germline. *Nat. Phys.* **17**, 920–925 (2021). <https://doi.org/10.1038/s41567-021-01235-x>
12. M. Mittasch, P. Gross, M. Nestler et al., Non-invasive perturbations of intracellular flow reveal physical principles of cell organization. *Nat. Cell Biol.* **20**, 344–351 (2018). <https://doi.org/10.1038/s41556-017-0032-9>
13. M. Mittasch, V.M. Tran, M.U. Rios et al., Regulated changes in material properties underlie centrosome disassembly during mitotic exit. *J. Cell Biol.* (2020). <https://doi.org/10.1083/jcb.201912036>
14. K. Kruse, N. Chiaruttini, A. Roux, Optical control of cytoplasmic flows. *Nat. Cell Biol.* **20**, 227–228 (2018). <https://doi.org/10.1038/s41556-018-0050-2>
15. T. Nawy, Live-streaming the cytoplasm. *Nat. Methods* **15**, 244–244 (2018). <https://doi.org/10.1038/nmeth.4656>
16. E. Erben, B. Seelbinder, I.D. Stoev et al., Feedback-based positioning and diffusion suppression of particles via optical control of thermoviscous flows. *Opt. Express* **29**, 30272 (2021). <https://doi.org/10.1364/OE.432935>
17. I.D. Stoev, B. Seelbinder, E. Erben et al., Highly sensitive force measurements in an optically generated, harmonic hydrodynamic trap. *eLight* **1**, 7 (2021). <https://doi.org/10.1186/s43593-021-00007-7>
18. X. Zhang, B. Gu, C.-W. Qiu, Force measurement goes to femto-Newton sensitivity of single microscopic particle. *Light Sci. Appl.* **10**, 243 (2021). <https://doi.org/10.1038/s41377-021-00684-6>
19. E.P. Armour, D. McEachern, Z. Wang et al., Sensitivity of human cells to mild hyperthermia. *Cancer Res.* **53**, 2740–2744 (1993)
20. T.W. Iorizzo, P.R. Jermain, E. Salomatina et al., Temperature induced changes in the optical properties of skin in vivo. *Sci. Rep.* **11**, 754 (2021). <https://doi.org/10.1038/s41598-020-80254-9>

21. S. Cho, M.H. Shin, Y.K. Kim et al., Effects of infrared radiation and heat on human skin aging in vivo. *J. Investig. Dermatol. Symp. Proc.* **14**, 15–19 (2009). <https://doi.org/10.1038/jidsymp.2009.7>
22. J. Hendrey, I. Kola, Thermolability of mouse oocytes is due to the lack of expression and/or inducibility of Hsp70. *Mol. Reprod. Dev.* **28**, 1–8 (1991). <https://doi.org/10.1002/mrd.1080280102>
23. S. Yang, D. Li, L. Feng et al., Transcriptome analysis reveals the high temperature induced damage is a significant factor affecting the osmotic function of gill tissue in Siberian sturgeon (*Acipenser baerii*). *BMC Genomics* **24**, 2 (2023). <https://doi.org/10.1186/s12864-022-08969-9>
24. A. Haji-Sheikh, F. de Monte, J.V. Beck, Temperature solutions in thin films using thermal wave Green's function solution equation. *Int. J. Heat Mass Transf.* **62**, 78–86 (2013). <https://doi.org/10.1016/j.jheatmasstransfer.2013.02.036>
25. Z. Zhu, H. Fan, J. Hua, C. Zhang, A Green's function solution to the transient heat transfer through the building wall. *Adv. Mech. Eng.* **8**, 168781401663657 (2016). <https://doi.org/10.1177/1687814016636572>
26. J. Choi, H. Zhou, R. Landig et al., Probing and manipulating embryogenesis via nanoscale thermometry and temperature control. *Proc. Natl. Acad. Sci.* **117**, 14636–14641 (2020). <https://doi.org/10.1073/pnas.1922730117>
27. B. Kyoo Park, N. Yi, J. Park et al., Thermal conductivity of bovine serum albumin: a tool to probe denaturation of protein. *Appl. Phys. Lett.* **99**, 163702 (2011). <https://doi.org/10.1063/1.3652704>
28. A.R.N. Bastos, C.D.S. Brites, P.A. Rojas-Gutierrez et al., Thermal properties of lipid bilayers determined using upconversion nanothermometry. *Adv. Funct. Mater.* **29**, 1905474 (2019). <https://doi.org/10.1002/adfm.201905474>
29. S.M. Hirsch, S. Sundaramoorthy, T. Davies et al., FLIRT: fast local infrared thermogenetics for subcellular control of protein function. *Nat. Methods* **15**, 921–923 (2018). <https://doi.org/10.1038/s41592-018-0168-y>
30. A.W. Fritsch, A.F. Diaz-Delgado, O. Adame-Arana et al., Local thermodynamics govern formation and dissolution of *Caenorhabditis elegans* P granule condensates. *Proc. Natl. Acad. Sci.* **118**, e2102772118 (2021). <https://doi.org/10.1073/pnas.2102772118>
31. C.P. Brangwynne, C.R. Eckmann, D.S. Courson et al., Germline P granules are liquid droplets that localize by controlled dissolution/condensation. *Science* (80–) **324**, 1729–1732 (2009). <https://doi.org/10.1126/science.1172046>
32. B. Seelbinder, M. Jain, E. Erben, et al., Non-invasive chromatin deformation and measurement of differential mechanical properties in the nucleus. *bioRxiv* 2021.12.15.472786. (2021) <https://doi.org/10.1101/2021.12.15.472786>
33. C.J. Chan, W. Li, G. Cojoc, J. Guck, Volume transitions of isolated cell nuclei induced by rapid temperature increase. *Biophys. J.* **112**, 1063–1076 (2017). <https://doi.org/10.1016/j.bpj.2017.01.022>
34. G. Perrella, A. Zioutopoulou, L.R. Headland, E. Kaiserli, The impact of light and temperature on chromatin organization and plant adaptation. *J. Exp. Bot.* **71**, 5247–5255 (2020). <https://doi.org/10.1093/jxb/eraa154>
35. M.R. Reichl, D. Braun, Thermophoretic manipulation of molecules inside living cells. *J. Am. Chem. Soc.* **136**, 15955–15960 (2014). <https://doi.org/10.1021/ja506169b>
36. Y. Kotsuchibashi, Recent advances in multi-temperature-responsive polymeric materials. *Polym. J.* **52**, 681–689 (2020). <https://doi.org/10.1038/s41428-020-0330-0>
37. M. Hippler, E. Blasco, J. Qu et al., Controlling the shape of 3D microstructures by temperature and light. *Nat. Commun.* **10**, 232 (2019). <https://doi.org/10.1038/s41467-018-08175-w>
38. B. Drobot, J.M. Iglesias-Artola, K. Le Vay et al., Compartmentalised RNA catalysis in membrane-free coacervate protocells. *Nat. Commun.* **9**, 3643 (2018). <https://doi.org/10.1038/s41467-018-06072-w>
39. M. Saito, D. Hess, J. Eglinger et al., Acetylation of intrinsically disordered regions regulates phase separation. *Nat. Chem. Biol.* **15**, 51–61 (2019). <https://doi.org/10.1038/s41589-018-0180-7>
40. C. Iserman, C. Desroches Altamirano, C. Jegers et al., Condensation of Ded1p promotes a translational switch from housekeeping to stress protein production. *Cell* **181**, 818–831.e19 (2020). <https://doi.org/10.1016/j.cell.2020.04.009>
41. J.M. Iglesias-Artola, B. Drobot, M. Kar et al., Charge-density reduction promotes ribozyme activity in RNA-peptide coacervates via RNA fluidization and magnesium partitioning. *Nat. Chem.* **14**, 407–416 (2022). <https://doi.org/10.1038/s41557-022-00890-8>
42. E. de Nadal, G. Ammerer, F. Posas, Controlling gene expression in response to stress. *Nat Rev Genet* **12**, 833–845 (2011). <https://doi.org/10.1038/nrg3055>
43. Z. Xing, A. Caciagli, T. Cao et al., Microrheology of DNA hydrogels. *Proc. Natl. Acad. Sci.* **115**, 8137–8142 (2018). <https://doi.org/10.1073/pnas.1722206115>
44. I.D. Stoev, T. Cao, A. Caciagli et al., On the role of flexibility in linker-mediated DNA hydrogels. *Soft Matter* **16**, 990–1001 (2020). <https://doi.org/10.1039/C9SM01398A>
45. A. Borštnik, H. Stark, S. Žumer, Temperature-induced flocculation of colloidal particles immersed into the isotropic phase of a nematic liquid crystal. *Phys. Rev. E* **61**, 2831–2839 (2000). <https://doi.org/10.1103/PhysRevE.61.2831>
46. S.O. Ilyina, T.S. Anokhina, S.O. Ilyin, Non-solvent- and temperature-induced phase separations of poly(lauro)lactam solutions in benzyl alcohol as methods for producing microfiltration membranes. *Colloids Interfaces* **7**, 10 (2023). <https://doi.org/10.3390/colloids7010010>
47. F. Tanaka, T. Koga, H. Kojima, F.M. Winnik, Hydration and phase separation of temperature-sensitive water-soluble polymers. *Chin. J. Polym. Sci.* **29**, 13–21 (2011). <https://doi.org/10.1007/s10118-010-1018-2>
48. M. Fränzl, F. Cichos, Hydrodynamic manipulation of nano-objects by optically induced thermo-osmotic flows. *Nat Commun* **13**, 656 (2022). <https://doi.org/10.1038/s41467-022-28212-z>
49. B. Ciraulo, J. Garcia-Guirado, I. de Miguel et al., Long-range optofluidic control with plasmon heating. *Nat. Commun.* **12**, 2001 (2021). <https://doi.org/10.1038/s41467-021-22280-3>
50. G. Baffou, F. Cichos, R. Quidant, Applications and challenges of thermo-plasmonics. *Nat. Mater.* **19**, 946–958 (2020). <https://doi.org/10.1038/s41563-020-0740-6>
51. Y. Qian, S.L. Neale, J.H. Marsh, Microparticle manipulation using laser-induced thermophoresis and thermal convection flow. *Sci. Rep.* **10**, 19169 (2020). <https://doi.org/10.1038/s41598-020-76209-9>
52. S. Nagelberg, J.F. Totz, M. Mittasch et al., Actuation of Janus emulsion droplets via optothermally induced marangoni forces. *Phys. Rev. Lett.* **127**, 144503 (2021). <https://doi.org/10.1103/PhysRevLett.127.144503>
53. D. Ershov, M.-S. Phan, J. W. Pylvänäinen, et al., Bringing TrackMate into the era of machine-learning and deep-learning. *bioRxiv* 2021.09.03.458852. (2021) <https://doi.org/10.1101/2021.09.03.458852>
54. J. Rodriguez, F. Peglion, J. Martin et al., aPKC Cycles between functionally distinct PAR protein assemblies to drive cell polarity. *Dev. Cell* **42**, 400–415.e9 (2017). <https://doi.org/10.1016/j.devcel.2017.07.007>
55. W. Thielicke, E. Stamhuis, PIVlab-towards user-friendly, affordable and accurate digital particle image velocimetry in MATLAB. *J. Open Res. Softw.* **2**, e30 (2014)
56. C. M. Gallo, J. T. Wang, F. Motegi, G. Seydoux, Cytoplasmic partitioning of P granule components is not required to specify the germline in *C. elegans*. *Science* **330**, 1685–1689 (2010). <https://doi.org/10.1126/science.1193697>